

Single MoS₂-flake as a high TCR non-cryogenic bolometer

Saba M. Khan^{1,2}, Jyoti Saini¹, Anirban Kundu¹, Renu Rani¹ and Kiran S. Hazra^{1,*}

¹Institute of Nano Science and Technology, Knowledge City, Sector 81, Mohali, Punjab 140306, India

²Department of Physics, Lancaster University, Lancaster, LA1 4YB, United Kingdom

*Corresponding email: kiran@inst.ac.in

Abstract

Temperature coefficient of resistance (TCR) of a bolometer can be tuned by modifying the thermal conductance of an absorbing materials since they sense radiations via the temperature change in the absorber. However, the thermal conductance of the absorber can be reduced by engineering the appropriate thermal isolation, which can be an ultimate solution towards making a highly sensitive thermal detector. Here, we have developed an atomically thin 2D bolometer detector made up of a mechanically transferred suspended multilayer-MoS₂ flake, eliminating the use of challenging thin-film fabrication process. The strength of our detector lies on the two factors: its large surface-to-volume window to absorb the radiations; the suspended configuration which prevents the heat dissipation through the substrate and therefore reduces the thermal conductance. The bolometric response of the detector is tested in both modes, via the photoresponse and the thermal response. The prototype is found to exhibit a very high TCR $\sim -9.5\%/K$ with the least achievable thermal noise-equivalent power (NEP) $\sim 0.61 \text{ pWHz}^{-1/2}$, in ambient conditions at 328 K.

Keywords: Bolometers, Temperature co-efficient of resistance (TCR), Thermal conductance, 2D materials, IR detection, MoS₂

Introduction

Non-cryogenic bolometers are highly demanded due to their evolving applications in defense, security, surveillance, astronomy, tomography and smart energy systems,¹⁻⁶ which requires a temperature sensing material with a high temperature coefficient of resistance (TCR) and low $1/f$ noise properties without requiring any cooling module. However, for the room-temperature bolometers, achieving high TCR with a substantial signal-to-noise ratio has always been a challenging task.⁷⁻¹⁰ In addition, the geometry of the absorber material is a crucial parameter that suffers major technological barriers for thin film based bolometer where fragile amorphous films are deposited in multilayer stacking.^{11,12} However, after the emergence of 2D layered materials, new possibilities have emerged where the active material itself can act as an absorber due to their large aspect ratio and single-crystallinity. These materials can mechanically be transferred and suspended between pre-patterned electrodes in a free-standing stable condition to achieve the desired thermal isolation.^{13,14} However, relentless efforts are made to develop non-cryogenic bolometers attaining high TCR based on graphene derivatives,¹⁵⁻¹⁷ but the ultimate limitation with graphene is its metallic nature and vanishingly small electron-phonon coupling at room temperature which restraint the-heat dissipation paths for electrons.¹⁸⁻²⁰ In this context, MoS₂ may prove to be an excellent candidate because of its semiconducting nature where the band gap is tuned with its layer numbers,²¹ and also offers the carriers concentration dependent electronic and optical properties.²² Besides, its phonon wavelength is compatible with the electronic transitions in momentum space, providing a superior electron-phonon coupling compared to other 2D materials.²³ Although, the electron-phonon coupling can further be enhanced by selecting a multilayer MoS₂ flake and becomes more robust with the increase in layer numbers via indirect band transition.^{24,25}

We here demonstrate the bolometric effect in a single multilayer MoS₂ flake in ambient conditions, where a decent TCR with significantly low thermal noise-equivalent power (NEP) has been achieved. The atomically thin bolometer prototype exhibits fairly high responsivity upon IR illumination with ultrashort response time, where thermal isolation is achieved by engineering a suspended structure.¹³ Our findings indicate that the massive absorption enabled by the large aspect ratio and the reduced thermal conductance due to suspended geometry are the key attributes in obtaining the profound bolometric response in the present configuration of the 2D MoS₂

bolometer. In addition, the thermal conductivity of the suspended MoS₂ flake is extracted utilizing the bolometric technique; putting forward a non-destructive technique to study the temperature-dependent transport properties in MoS₂-based devices.

Results and Discussion

The AFM height image of the suspended MoS₂ device is shown in **Figure 1a**, which is fabricated by mechanically transferring a MoS₂ flake on to the pre-patterned two gold electrodes on a Si/SiO₂ substrate. The inset is showing the layer thickness along the white dotted line in the main figure, the thickness of the flake is found to be ~ 103 nm which gives an idea of approximate layer numbers of ~ 150 when consider the interlayer spacing of ~ 0.6 - 1 nm.^{26,27} The multilayer behavior of the flake can also be verified with its Raman spectra (**Figure 1b**), obtained at ambient conditions by utilizing the 532 nm laser line with a laser spot of ~ 1 μ m. The two Raman active modes, E_{2g}¹ at ~ 383.4 cm⁻¹ and A_{1g} at ~ 408.5 cm⁻¹ appear in the spectra, which corresponds to in-plane Mo-S opposite vibration and out-of-plane S-S relative vibration, respectively. The difference between these two peak positions is found to be ~ 25.1 cm⁻¹, which depicts its multilayer arrangement as reported previously.²⁸

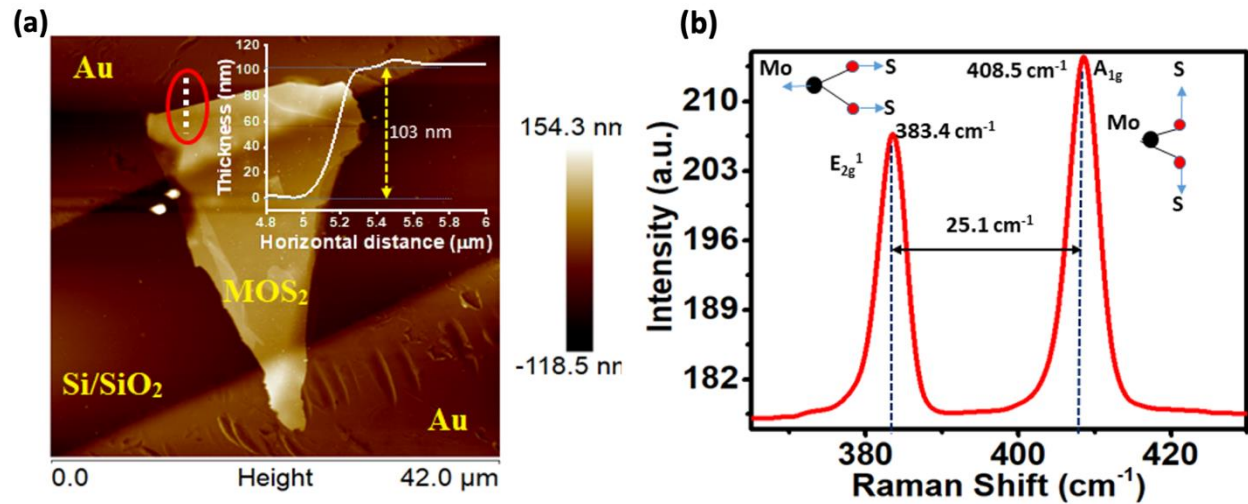


Figure 1. (a) AFM height image of the as-fabricated device; the thickness of the MoS₂ flake is found to be ~ 103 nm which confirms a multilayer stacking of MoS₂. (b) Raman spectra of the MoS₂ contains both the characteristic Raman peaks corresponding to in-plane and out-of-plane modes, with the expected separation of ~ 25 cm⁻¹ in the multilayer stacks.

In order to probe the bolometric response of the suspended MoS₂ flake, an indigenous optical arrangement has been designed with a monochromatic light source with spectral resolution ~ 0.4 nm and an optical chopper. **Figure S1** (Supplementary Information) shows the schematic of the experimental set-up used to perform the measurements, where the electrical response in the device upon light irradiation of tunable wavelengths and powers are obtained using a standard Keithley source meter. A single NIR line of 900 nm (~ 1.38 eV) with ~ 5 μ W is irradiated on the device, while the excitation energy ~ 1.38 eV is deliberately kept lower than the optical band gap of the MoS₂ to avoid the photoconductive effect.^{21,26,29,30} Furthermore, the possibility of photo-response from the thermoelectric effect is also eliminated by uniform exposure of NIR radiation on the whole device area. The chopping frequency is kept as low as 40 Hz to get the longer exposure time of NIR radiations onto the sample and thus achieving the saturation current to determine the sensitivity (S) and response time (τ) of the detector.

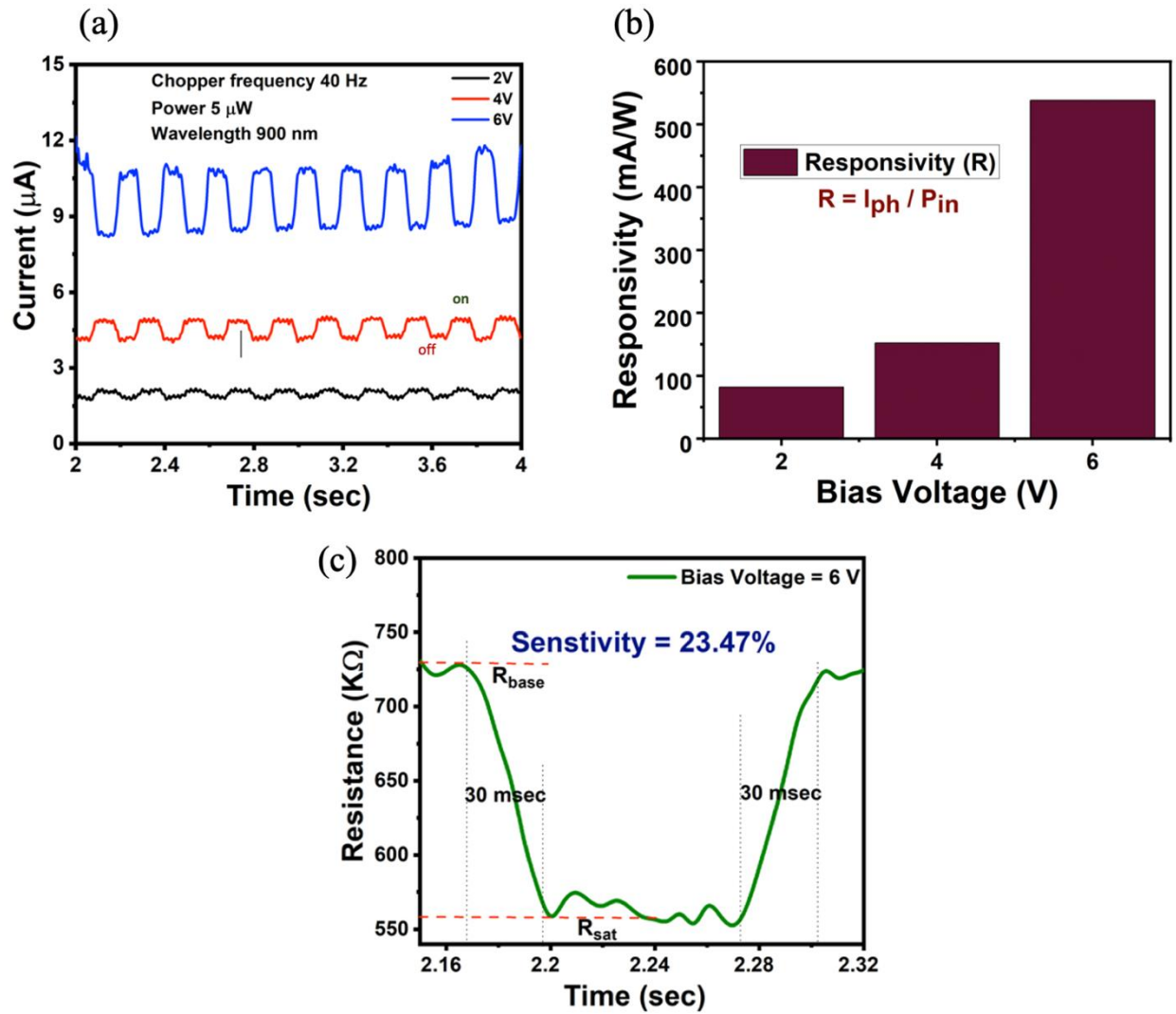


Figure 2. (a) IR response of MoS_2 device for three constant bias-voltages at 40Hz chopping frequency. The detector shows a sharp increase in the current when exposed to radiations, whilst the current is rising with the applied bias. (b) Bias voltage dependence of responsivity for the suspended detector; sees a ~ 7 folds rise in the responsivity when a bias voltage is increased from 2V to 6V. (c) Resistance variation of the MoS_2 on illuminating with an IR beam at constant bias voltage of 6V, presents the response time of the device with baseline resistance and saturated resistance. The device exhibits a very short response and recovery times (~ 30 ms) with fairly high sensitivity.

The change in electrical response with the applied light pulses of 40 Hz (pulse width ~ 25 msec) has been depicted in **Figure 2a**, which shows a sharp change in the channel current upon light irradiation. To improve the signal-to-noise ratio (SNR), the change in electrical response have been

recorded with different applied bias, i.e., 2, 4 and 6 V, where the substantial increment is observed at 6 V. The increase in applied bias clearly improves the SNR (**Figure 2a**), which shows that at a constant bias of 6 V, a sharp and distinguishable change in electrical response is obtained. **Figure 2a** depicts the generation of periodic pulses of change in current with identical periodicity upon switching on the incident NIR pulses on the device. Upon switching on the NIR pulse, the current enhances rapidly and achieves the saturation followed by a sharp drop when switched off. The plot shows that the baseline and the saturation line are almost parallel, indicating that the changes were solely due to incident radiation.^{31,32} The current responsivity (R) of the device has been determined using the equation, $R = \frac{I_{ph}}{P_{in}}$, where I_{ph} and P_{in} are the current under illumination and incident power, respectively. Responsivity of the device has been measured with varying applied bias (**Figure 2b**), which shows a significant improvement in the responsivity with increasing the applied bias. For an instance, the responsivity ~ 538 mA/W is obtained at applied bias 6V, which shows a ~ 7 -fold enhancement as compare to the responsivity (~ 78 mA/W) at 2 V. Such higher responsivity of the device indicates its potential for using the micro-bolometer even at very low radiation power. Furthermore, the sensitivity (S) of the micro-bolometer device has been measured using the equation, $S = \frac{R_{base} - R_{sat}}{R_{base}} \times 100\%$, where R_{base} and R_{sat} are the base and saturation resistances, respectively. The change in resistance upon single pulse light irradiation at an applied bias 6 V is plotted in **Figure 2c**, which clearly depicts that the resistance sharply drops from its initial value ~ 729 k Ω at dark condition to ~ 558 k Ω upon light irradiation. Such sharp change in resistance offers a sensitivity (S) of $\sim 23.47\%$ at room temperature with ~ 5 μ W power, which confirms the resolving capability with lower temperature fluctuation of the suspended MoS₂ at non-cryogenic temperature. The response time (τ) is determined by considering the time needed to change from 10% to 90% decrease in resistance, which is defined as $\tau = \frac{C}{G}$, where C is the specific heat capacity of material and G is thermal conductance. In **Figure 2c**, both the growth and decay response time has been obtained as ~ 30 msec, which is much slower as compared to the previously reported response time originated due to photocurrent generation, which confirms the bolometric response in the device.¹⁰

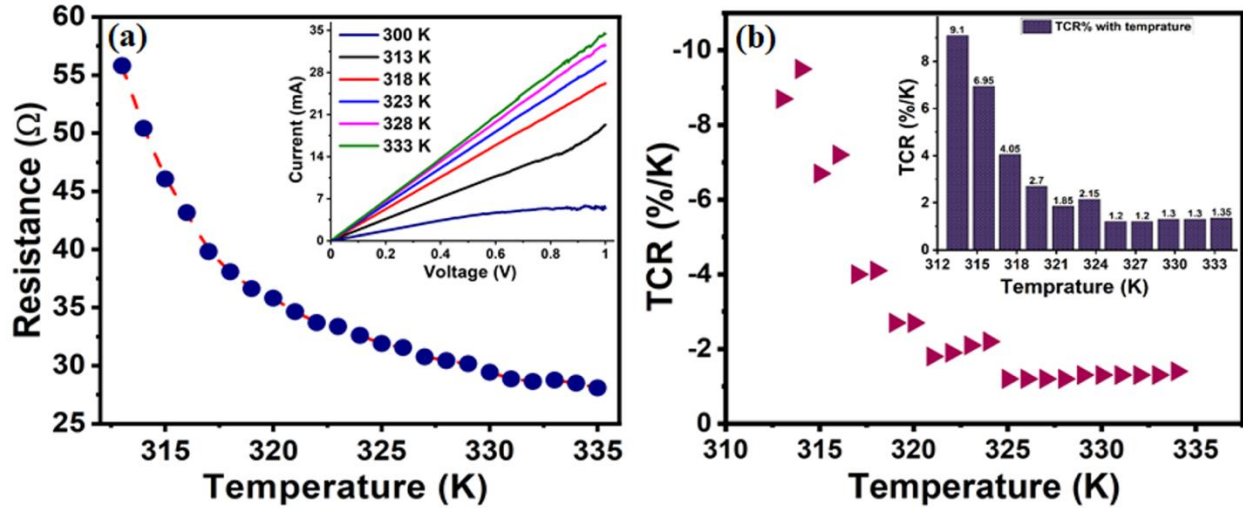


Figure 3. (a) Resistance variation for the temperature range from 312K to 335K: The resistance of the device starts to decrease as we increase its temperature, and such a sharp variation in resistance with the temperature is a measure of the highly sensitive bolometric detection. **Inset:** I-V characteristics at different temperatures where current through the detector is increasing rapidly with the increase in temperature. (b) The percentage TCR against the temperature change: The device TCR is extracted via Eq.4 and is plotted as a function of temperature. Initially, the TCR is seeing a sharp decline with the temperature rise, but it starts to saturate at beyond 325K. **Inset:** the histogram of measured TCR versus device temperature.

Although we have eliminated the possibility of inter-band transition by irradiation with lower energy wavelength than the band gap, yet to further confirm the bolometric response, the device is heated isothermally on a hot plate and corresponding electrical response is recorded to investigate the temperature response of the micro-bolometer (the suspended MoS₂ flake). In **Figure 3a**, we have plotted the change in resistance of the micro-bolometer with the increase in temperature, which shows exponential decay in resistance with the increase in temperature. The I-V responses with varying temperature are recorded by using two-probe method at normal atmospheric pressure with the change in substrate temperature, recorded by a J-type thermocouple having a swept from 40 °C to 62 °C in step of 1 °C (**inset of Figure 3a**). With the increase in temperature of the micro-bolometer device, a gradual rise in conductivity is observed which is originated due to the semiconducting nature of the MoS₂ flake.³³ However, the heat sensitivity of the suspended flake can be directly estimated by extracting its temperature coefficient of resistance

(TCR), which is a key figure of merit of a micro-bolometer since it determines the rate of change in resistivity with temperature. In normalized form, at a particular temperature the TCR is defined as

$$TCR (\alpha) = \frac{1}{R} \left(\frac{dR}{dT} \right) \quad (1)$$

Which predicts that the materials having high TCR offer large sensitivity (S) and so are suitable for bolometric application^[34]. Using equation 1, the TCR is plotted in **Figure 3b** at non-cryogenic temperatures varying from 313K to 333K. The maximum TCR value is found to be $\sim -9.5\%/K$ at 314 K, which is significantly higher than that of the commercially available state-of-art non-cryogenic bolometers within the range of 0.01–3%/K.³⁵⁻⁴⁰ Such high TCR of the device can be attributed due to the large effective surface area of the MoS₂. In earlier reports,^{31,34,41} it is anticipated that the improvement in the TCR at cryogenic temperature can further be demonstrated by fabricating the cavity-like structure due to the enhanced infrared absorption, therefore, the suspended MoS₂ flake as a micro-bolometer may pave a path towards the development of next-generation bolometric sensors at non-cryogenic temperature.

In order to understand the mechanism behind the enhancement in current upon NIR irradiation, firstly the possibility of thermoelectric effect can be discarded as the experimental set-up provides uniform illumination/heating of the sample. The charge carriers (electrons in this case) gain some thermal energy from this uniform heating process during NIR illumination, which would equally be distributed among the charge carriers. Such uniform enhancement in the electron temperature leads to the reduction in the mean free path, and consequently a significant drop in the materials resistivity is observed. We have attributed this profound change in the resistivity to the suspended geometry of our device, where the electrons cannot dissipate their thermal energy towards the substrate which result in the increment of channel resistance.

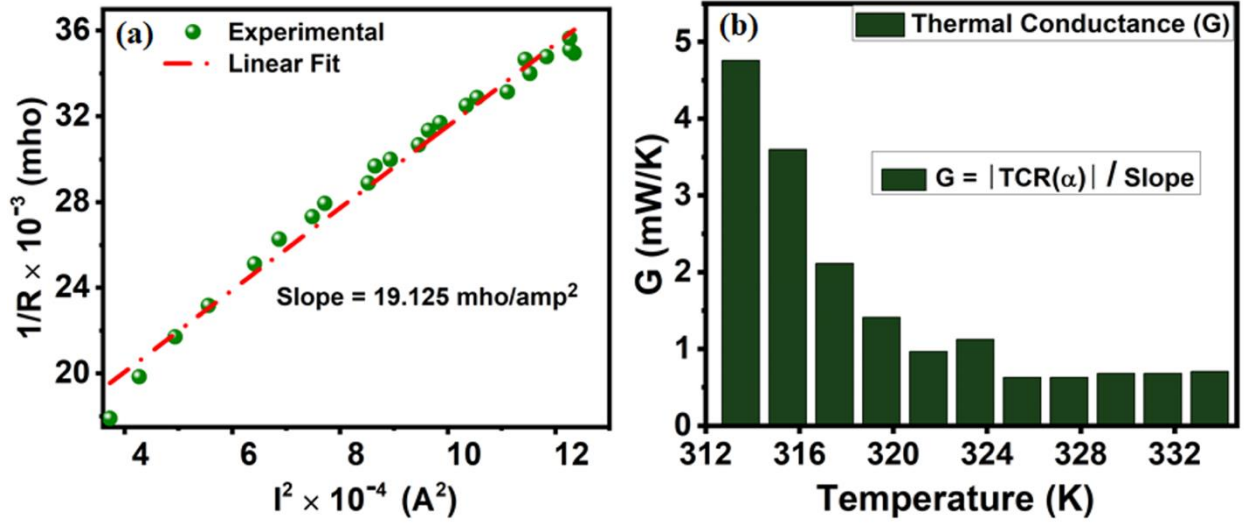


Figure 4. (a) The $1/R$ against the square of the current is plotted, where the slope of the fit provides the TCR to thermal conductance ratio using equation 6. (b) The thermal conductance of the MoS2 device is extracted from the slope of (a) and is presented as a function of temperature. At first, the device conductance is reducing as temperature rises and then starts to plateau at 325K.

The bolometric response of a device has a direct dependency on the thermal conductance of the active materials, i.e., $G = \frac{dP}{dT}$, or equivalent thermal resistance $R_h = dT/dP$, which quantifies the thermal response of the material upon incident radiation power (P).^[41] To characterize the quantitative thermal conductance (or thermal resistance), we have assumed that the heat conduction is only possible through the supporting gold electrodes^[42] for corresponding heat loss due to the Joule heating. Thus, the corresponding dissipated power will be equivalent to the thermal loss and can be defined as-

$$I^2 R = G (T - T_0) \quad (2)$$

Now, comparing the $(T-T_0)$ or dT values in equations (1) and (2), we have obtained

$$\frac{1}{R} = \frac{1}{R_0} - \left(\frac{\alpha}{G}\right) I_2 \quad (3)$$

The Eq.3 implies that $1/R$ varies linearly with the I^2 , and the slope of the fitted curve can be used to derive α/G ratio. The slope of the plot in **Figure 4a** curve has been used to extract the behavior of thermal conductance G of the device with temperature (**Figure 4b**), where the TCR (α) values are taken from **Figure 3b**. **Figure 4b** shows the behavior of thermal conductance of the bolometer

with temperature change; the thermal conductance associated with the maximum TCR at 314 K is found to be ~ 5 mW/K, which has been reduced rapidly to ~ 0.63 mW/K at 328 K. By knowing the values of response time τ and G , one may easily find the specific heat capacity C of the multilayer flake using equation $\tau = \frac{C}{G}$, which is $\sim 1.88 \times 10^{-6}$ Joule per Kelvin at 328 K. Thermal and electrical properties of MoS₂ can be studied by analyzing the joule heating mechanism via the thermal conductance in the suspended bolometer, which is a major contribution of this work. Here, we introduce a novel technique to measure the thermal conductivity (κ) of the MoS₂ flake by utilizing the bolometric effect instead of Raman thermometry which has limited scope for the materials with less sensitive Raman peaks to the temperature variations. As we know thermal conductance of any nanomaterial is given by $G = A\kappa/(dx)$, where A is the area of the nanomaterial, κ is the thermal conductivity and dx is thickness of the nanomaterial. In our device thickness (dx) of MoS₂ flake is ~ 103 nm and calculated area is $\sim 30 \mu\text{m}^2$. We can calculate the thermal conductivity (κ) if the thermal conductance (G) of nanomaterial is known. Using the above calculated thermal conductance of MoS₂ flake via bolometric effect, the extracted thermal conductivity at 314 K is ~ 17.17 W/mK, which is lower as compared to the previously reported thermal conductivity of the suspended few-layer MoS₂ flake.⁴³ This discrepancy can be explained in terms of the variation in the thermal conductivity with the MoS₂ flake thickness, the thermal conductivity of MoS₂ decreases as we increase the layer numbers.⁴⁴ Therefore, this single device can be used to extract all the transport properties in the multilayer MoS₂.

Following the thermal conductance measurement, the signal-to-noise ratio of the detector is estimated which is a measure of the detectivity of a detector. However, the high signal-to-noise ratio of bolometer detectors yields low noise-equivalent power (NEP). In a measurement set-up, many noise sources could be present such as those from the amplifiers,^{34,45,46} but some are inherent to the bolometer itself namely the Johnson–Nyquist noise and the thermal fluctuations.³⁴ The

Johnson–Nyquist noise can be determined from the expression $\sqrt{\frac{4kBT}{R_{res}}}$, which turns out to be ~ 43.04 pWHz^{-1/2} for R_{res} 538 mA/W at 328 K. However, the thermal fluctuation NEP directly depends on the thermal conductance (G) and the temperature (T) of the bolometer and is defined as $\sqrt{(4kBT^2G)}$.⁴⁵ At 328 K, the NEP due to thermal noise is ~ 0.61 pW Hz^{-1/2} corresponding to measured $G \sim 0.63$ mW/K. Therefore, the measured NEP of MoS₂ microbolometer from the

intrinsic noise sources is remarkably low in-contrast to the so far existing non-cryogenic bolometers^[16], this signifies the novelty of our detector with its large signal-to-noise ratio. The intrinsic *NEP* can further be improved by reducing the thermal loss of the IR absorbing material and by increasing the responsivity. The **Table 1** given below shows the comparison of *TCR* of our suspended MoS₂ device with the other previously reported devices.

Table 1. TCR values of available non-cryogenic bolometer detectors

Sl. No.	Detector Type	TCR value	Reference
1	Graphene	≈ 11% /K at 296 K	10
2	Reduced Graphene Oxide	≈ 44×10 ³ Ω/K at 60K	38
3	Ti	≈ 0.27% /K	44
4	Graphene Aerogel	≈ 0.3% /K at 295 K, ≈ 2.9%/K at 10 K	15
5	SWCNT	≈ 2.94% /K at 300 K	45
6	VOx	≈ 2.1%/K at 298 K	46
7	MoS ₂	≈ 9.5% /K at 314 K	Present Work

Furthermore, we have developed a single pixel prototype of thermal sensor (designed on the Arduino platform) based on an equivalent suspended MoS₂ micro-bolometer, as shown in the circuit diagram of **Figure 5a**. User-contributed function libraries like PWM control, I2C and SPI are used to program the Arduino board.

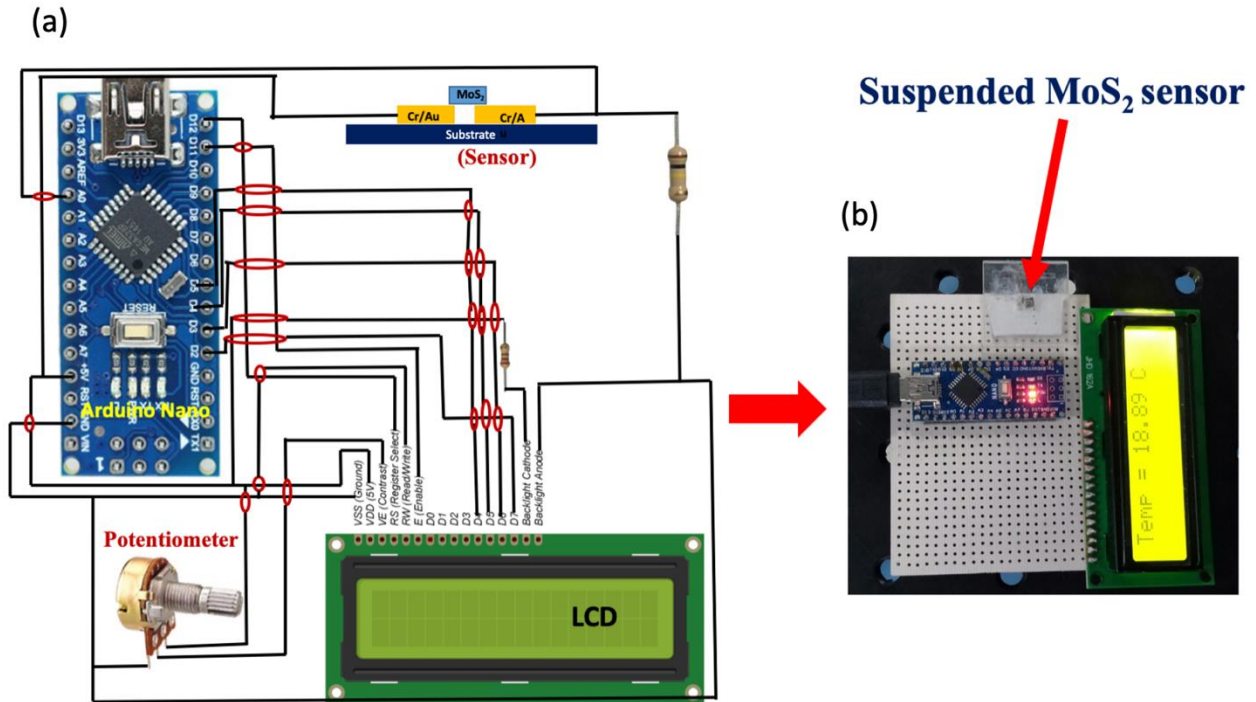


Figure 5. (a) Circuit diagram of the suspended MoS₂flake-based prototype bolometer, designed on the Arduino platform where an LCD is used to directly demonstrate the temperature variation of the detector upon IR irradiation. (b) Real image of our prototype assembled on a breadboard: the detector is mounted on a glass slide and soldered to a Nano Arduino along with a LCD.

During the IR irradiation on the MoS₂ micro-bolometer, the temperature variation caused by the radiation exposure led to the change in the resistance of the sensor which is recorded through the digital pins of the Arduino and matches with the pre-calibrated database of the current response with temperature. Microcontroller board of the Arduino then processes these signals as per the given coding and sends them to the sensor's output through its analogue pin to display it on the LCD screen, as demonstrated in **Figure 5b**. Hence, the suspended multilayer MoS₂, which is thermally isolated from the substrate to reduce the heat loss, can be a promising material for the future non-cryogenic bolometer technology concerned to the thermal detection.

Conclusion

We have investigated the non-cryogenic bolometric response in a suspended multilayer MoS₂-flake, where its free-standing architecture eliminates the heat exchange possibility with the substrate and results in the high-yield conversion of the absorbed energy into an electrical signal.

Such higher absorption capability leads to the maximum achievable TCR of $-9.5\%/K$ at 314K, which is much higher than the commercially available Si or VO_x based non-cryogenic bolometers. Furthermore, the thermal conductance G , which limits the speed of the bolometer, is found to be fairly low (~ 4.97 mW/K at 314K), and consequently, the device has least thermal NEP of 0.61 $\text{pW Hz}^{-1/2}$ at 328K with the Johnson noise of ~ 43.04 $\text{pW Hz}^{-1/2}$. Finally, a prototype of single pixel temperature sensor has been proposed which can sense small energy differences like IR-radiations. Since the heat loss prevails through the gold electrodes of the suspended device, the optimized gold electrode's structure may elevate the MoS_2 -based future bolometric devices. Also, the sensitivity of the sensor may further be upgraded by enhancing the absorption of the incident radiations by fabricating the micro (or) nano cavities.

Experimental Details:

The suspended MoS_2 devices are fabricated with photolithography by writing a rectangular pattern of electrodes on a 290 nm-thick SiO_2 substrate underlying the highly doped p-type Silicon. Subsequently, the electron beam deposition technique is used to deposit a stack of Cr/Au (10/60nm) on these pre-written electrodes. Then, the micromechanical exfoliation method is considered to transfer a multilayer MoS_2 flake onto the PDMS from a single crystal of MoS_2 , and finally, the flake is transferred from the PDMS onto the two rectangular gold electrodes separated by 20 μm gap using a home-built transfer stage.

Supporting Information

The Supporting Information includes the following details.

Figure S1. Photoluminescence (PL) spectra of MoS_2

Figure S2. I-V characteristic of MoS_2 device in dark indicating the ohmic behavior of the contact between flake and gold electrodes

Figure S3. Schematic diagram for MoS_2 device and measurement set-up

Figure S4. Band alignment of both suspended (a) and supported (b) MoS_2 device under IR illumination

Author Information

*Correspondence to be addressed to K.S.H (kiran@inst.ac.in)

Kiran Shankar Hazra - Institute of Nano Science and Technology, Knowledge City, Sector 81,
Mohali, Punjab-140306, India

Email: kiran@inst.ac.in

Author Contributions

S.M.K. and K.S.H. designed the experiments and S.M.K. performed all the measurements. S.M.K., A.K. analysed the data and prepare the original draft. J.S., A.K. and R.R did the formal analysis and data curation; K.S.H. supervised the research project and corrected the manuscript.

Acknowledgments

K.S.H. would like to acknowledge the grant sanctioned by the DST-SERB under EEQ scheme (Project No. EEQ/2017/000497). S.M.K. and J.S. would like to acknowledge the DST-SERB for their fellowship through the project grant (EEQ/2017/000497). S.M.K. would like to thank Mamta Raturi for the technical assistance with the AFM data and Saif Ali Khan for the fruitful discussion and comments on the manuscript.

References

- (1) Richards, P. L.; McCreight, C. R. Infrared Detectors for Astrophysics. *Phys. Today* **2005**, *58* (2), 41–47. <https://doi.org/10.1063/1.1897522>.
- (2) Jones, B. F. A Reappraisal of the Use of Infrared Thermal Image Analysis in Medicine. *IEEE Trans. Med. Imaging* **1998**, *17* (6), 1019–1027. <https://doi.org/10.1109/42.746635>.
- (3) Koh, A.; Gutbrod, S. R.; Meyers, J. D.; Lu, C.; Webb, R. C.; Shin, G.; Li, Y.; Kang, S. K.; Huang, Y.; Efimov, I. R.; Rogers, J. A. Ultrathin Injectable Sensors of Temperature, Thermal Conductivity, and Heat Capacity for Cardiac Ablation Monitoring. *Adv. Healthc. Mater.* **2016**, *5* (3), 373–381. <https://doi.org/10.1002/adhm.201500451>.
- (4) Meijer, G. C. M. (Gerard C. M. . *Smart Sensor Systems*; J. Wiley & Sons: Chichester, U.K. , 2008.
- (5) Rudol, P.; Doherty, P. Human Body Detection and Geolocalization for UAV Search and Rescue Missions Using Color and Thermal Imagery. *IEEE Aerosp. Conf. Proc.* **2008**. <https://doi.org/10.1109/AERO.2008.4526559>.
- (6) Simon, I.; Arndt, M. Thermal and Gas-Sensing Properties of a Micromachined Thermal Conductivity Sensor for the Detection of Hydrogen in Automotive Applications. *Sensors Actuators, A Phys.* **2002**, *97–98*, 104–108. [https://doi.org/10.1016/S0924-4247\(01\)00825-1](https://doi.org/10.1016/S0924-4247(01)00825-1).
- (7) Kruse, P. W.; Society of Photo-optical Instrumentation Engineers. *Uncooled Thermal Imaging : Arrays, Systems, and Applications*; SPIE, 2001.
- (8) Breen, T.; Butler, N.; Kohin, M.; Marshall, C. A.; Murphy, R.; Parker, T.; Piscitelli, N.; Silva, R. Summary of Applications of Uncooled Microbolometer Sensors. *IEEE Aerosp. Appl. Conf. Proc.* **1999**, *3*, 361–374. <https://doi.org/10.1117/12.328051>.
- (9) Ryzhii, V.; Otsuji, T.; Ryzhii, M.; Ryabova, N.; Yurchenko, S. O.; Mitin, V.; Shur, M. S. Graphene Terahertz Uncooled Bolometers. *J. Phys. D. Appl. Phys.* **2013**, *46* (6), 1–5. <https://doi.org/10.1088/0022-3727/46/6/065102>.
- (10) Yadav, A. K.; Khan, S. M.; Kundu, A.; Rani, R.; Soin, N.; McLaughlin, J.; Misra, D. S.; Hazra, K. S. Vertically Aligned Few-Layered Graphene-Based Non-Cryogenic Bolometer. *C* **2019**, *5* (2), 23. <https://doi.org/10.3390/c5020023>.
- (11) Niklaus, F.; Vieider, C.; Jakobsen, H. MEMS-Based Uncooled Infrared Bolometer Arrays: A Review. *MEMS/MOEMS Technol. Appl. III* **2007**, *6836*, 68360D. <https://doi.org/10.1117/12.755128>.
- (12) Butler, D. P.; Celik-Butler, Z. A Device-Level Vacuum-Packaging Scheme for Microbolometers on Rigid and Flexible Substrates. *IEEE Sens. J.* **2007**, *7* (7), 1012–1019. <https://doi.org/10.1109/JSEN.2007.896560>.

- (13) Cai, W.; Moore, A. L.; Zhu, Y.; Li, X.; Chen, S.; Shi, L.; Ruoff, R. S. Thermal Transport in Suspended and Supported Monolayer Graphene Grown by Chemical Vapor Deposition. *Nano Lett.* **2010**, *10* (5), 1645–1651. <https://doi.org/10.1021/nl9041966>.
- (14) Bolotin, K. I.; Sikes, K. J.; Hone, J.; Stormer, H. L.; Kim, P. Temperature-Dependent Transport in Suspended Graphene. *Phys. Rev. Lett.* **2008**, *101* (9), 1–4. <https://doi.org/10.1103/PhysRevLett.101.096802>.
- (15) Xie, Y.; Han, M.; Wang, R.; Zobeiri, H.; Deng, X.; Zhang, P.; Wang, X. Graphene Aerogel Based Bolometer for Ultrasensitive Sensing from Ultraviolet to Far-Infrared. *ACS Nano* **2019**, *13* (5), 5385–5396. <https://doi.org/10.1021/acsnano.9b00031>.
- (16) Blaikie, A.; Miller, D.; Alemán, B. J. A Fast and Sensitive Room-Temperature Graphene Nanomechanical Bolometer. *Nat. Commun.* **2019**, *10* (1), 1–8. <https://doi.org/10.1038/s41467-019-12562-2>.
- (17) Du, X.; Prober, D. E.; Vora, H.; Mckitterick, C. B. Graphene-Based Bolometers. *Graphene 2D Mater.* **2014**, *1* (1), 1–22. <https://doi.org/10.2478/gpe-2014-0001>.
- (18) Tse, W.-K.; Das Sarma, S. Energy Relaxation of Hot Dirac Fermions in Graphene. *Phys. Rev. B* **2009**, *79* (23), 235406. <https://doi.org/10.1103/PhysRevB.79.235406>.
- (19) Song, J. C. W.; Reizer, M. Y.; Levitov, L. S. Disorder-Assisted Electron-Phonon Scattering and Cooling Pathways in Graphene. *Phys. Rev. Lett.* **2012**, *109* (10), 1–5. <https://doi.org/10.1103/PhysRevLett.109.106602>.
- (20) Betz, A. C.; Jhang, S. H.; Pallecchi, E.; Ferreira, R.; Fève, G.; Berroir, J. M.; Plaçais, B. Supercollision Cooling in Undoped Graphene. *Nat. Phys.* **2013**, *9* (2), 109–112. <https://doi.org/10.1038/nphys2494>.
- (21) Fan, X.; Chang, C. H.; Zheng, W. T.; Kuo, J. L.; Singh, D. J. The Electronic Properties of Single-Layer and Multilayer MoS₂ under High Pressure. *J. Phys. Chem. C* **2015**, *119* (19), 10189–10196. <https://doi.org/10.1021/acs.jpcc.5b00317>.
- (22) Steinhoff, A.; Rösner, M.; Jahnke, F.; Wehling, T. O.; Gies, C. Influence of Excited Carriers on the Optical and Electronic Properties of MoS₂. *Nano Lett.* **2014**, *14* (7), 3743–3748. <https://doi.org/10.1021/nl500595u>.
- (23) Gunst, T.; Markussen, T.; Stokbro, K.; Brandbyge, M. First-Principles Method for Electron-Phonon Coupling and Electron Mobility: Applications to Two-Dimensional Materials. *Phys. Rev. B* **2016**, *93* (3), 1–14. <https://doi.org/10.1103/PhysRevB.93.035414>.
- (24) Mahatha, S. K.; Ngankeu, A. S.; Hinsche, N. F.; Mertig, I.; Guilloy, K.; Matzen, P. L.; Bianchi, M.; Sanders, C. E.; Miwa, J. A.; Bana, H.; Travaglia, E.; Lacovig, P.; Bignardi, L.; Lizzit, D.; Larciprete, R.; Baraldi, A.; Lizzit, S.; Hofmann, P. Electron-Phonon Coupling in Single-Layer MoS₂. **2018**.

<https://doi.org/10.1016/j.susc.2018.11.012>.

- (25) Bae, J. J.; Jeong, H. Y.; Han, G. H.; Kim, J.; Kim, H.; Kim, M. S.; Moon, B. H.; Lim, S. C.; Lee, Y. H. Thickness-Dependent in-Plane Thermal Conductivity of Suspended MoS₂ Grown by Chemical Vapor Deposition. *Nanoscale* **2017**, *9* (7), 2541–2547. <https://doi.org/10.1039/c6nr09484h>.
- (26) Lu, H.; Gan, X.; Mao, D.; Fan, Y.; Yang, D.; Zhao, J. Nearly Perfect Absorption of Light in Monolayer Molybdenum Disulfide Supported by Multilayer Structures. *Opt. Express* **2017**, *25* (18), 21630. <https://doi.org/10.1364/OE.25.021630>.
- (27) Li, X.; Zhu, H. Two-Dimensional MoS₂: Properties, Preparation, and Applications. *J. Mater.* **2015**, *1* (1), 33–44. <https://doi.org/10.1016/j.jmat.2015.03.003>.
- (28) Lee, C.; Yan, H.; Brus, L. E.; Heinz, T. F.; Hone, J.; Ryu, S. Anomalous Lattice Vibrations of Single- and Few-Layer MoS₂. *ACS Nano* **2010**, *4* (5), 2695–2700. <https://doi.org/10.1021/nn1003937>.
- (29) Park, J. W.; So, H. S.; Kim, S.; Choi, S.-H.; Lee, H.; Lee, J.; Lee, C.; Kim, Y. Optical Properties of Large-Area Ultrathin MoS₂ Films: Evolution from a Single Layer to Multilayers. *J. Appl. Phys.* **2014**, *116* (18), 183509. <https://doi.org/10.1063/1.4901464>.
- (30) Wang, Q.; Lai, J.; Sun, D. Review of Photo Response in s e Miconductor Transition Metal Dichalcogenides Based Photosensitive Devices. **2016**, *6* (7), 2313–2327. <https://doi.org/10.1364/OME.6.002313>.
- (31) Luo, S.; Qi, X.; Ren, L.; Hao, G.; Fan, Y.; Liu, Y.; Han, W.; Zang, C.; Li, J.; Zhong, J. Photoresponse Properties of Large-Area MoS₂ Atomic Layer Synthesized by Vapor Phase Deposition. *J. Appl. Phys.* **2014**, *116* (16), 164304. <https://doi.org/10.1063/1.4898861>.
- (32) Perry, M. D.; Mourou, G.; Maksimchuk, a; Gu, S.; Flippo, K.; Umstadter, D.; Malka, V.; Faure, J.; Glinec, Y.; Lifschitz, a F.; Ledingham, K. W. D.; Mckenna, P.; Shinghal, R. P.; Remington, B. a; Arnet, D.; Drake, R. P.; Takabe, H.; Bulanov, S. V; Khoroshkov, V. S.; Kuznetsov, a V; Pegoraro, F.; Szilagy, M.; Luo, W.; Fourkal, E.; Li, J.; Pukhov, a; Grismayer, T.; Gordienko, S.; Lefebvre, E.; Mora, P. Bolometric Infrared Photoresponse Of. **2006**, No. April, 413–416. <https://doi.org/10.1126/science.1125695>.
- (33) Mak, K. F.; Lee, C.; Hone, J.; Shan, J.; Heinz, T. F. Atomically Thin MoS₂ : A New Direct-Gap Semiconductor. *Phys. Rev. Lett.* **2010**, *105* (13), 136805. <https://doi.org/10.1103/PhysRevLett.105.136805>.
- (34) Mather, J. C. Bolometers: Ultimate Sensitivity, Optimization, and Amplifier Coupling. *Appl. Opt.* **1984**, *23* (4), 584. <https://doi.org/10.1364/AO.23.000584>.
- (35) Rao, F.; Liu, X.; Li, T.; Zhou, Y.; Wang, Y. The Synthesis and Fabrication of Horizontally Aligned Single-Walled Carbon Nanotubes Suspended across Wide Trenches for Infrared Detecting Application. *Nanotechnology* **2009**, *20* (5), 055501. <https://doi.org/10.1088/0957->

4484/20/5/055501.

- (36) Lu, R.; Shi, J. J.; Baca, F. J.; Wu, J. Z. High Performance Multiwall Carbon Nanotube Bolometers. *J. Appl. Phys.* **2010**, *108* (8), 084305. <https://doi.org/10.1063/1.3492633>.
- (37) Itkis, M. E.; Borondics, F.; Yu, A.; Haddon, R. C. Bolometric Infrared Photoresponse of Suspended Single-Walled Carbon Nanotube Films. *Science* **2006**, *312* (5772), 413–416. <https://doi.org/10.1126/science.1125695>.
- (38) Dickerson, W.; Hemsworth, N.; Gaskell, P.; Ledwosinska, E.; Szkopek, T. Bolometric Response of Free-Standing Reduced Graphene Oxide Films. *Appl. Phys. Lett.* **2015**, *107* (24). <https://doi.org/10.1063/1.4937928>.
- (39) Bachmann, R.; Kirsch, H. C.; Geballe, T. H. Low Temperature Silicon Thermometer and Bolometer. *Rev. Sci. Instrum.* **1970**, *41* (4), 547–549. <https://doi.org/10.1063/1.1684573>.
- (40) Kuzmin, L. S.; Devyatov, I. A.; Golubev, D. Cold-Electron Bolometer with Electronic Microrefrigeration and General Noise Analysis; Afsar, M. N., Ed.; International Society for Optics and Photonics, 1998; Vol. 3465, p 193. <https://doi.org/10.1117/12.331165>.
- (41) Alsop, D. C.; Inman, C.; Lange, A. E.; Wilbanks, T. Design and Construction of High-Sensitivity, Infrared Bolometers for Operation at 300 MK. *Appl. Opt.* **1992**, *31* (31), 6610. <https://doi.org/10.1364/AO.31.006610>.
- (42) Bhan, R. K.; Saxena, R. S.; Jalwania, C. R.; Lomash, S. K. Uncooled Infrared Microbolometer Arrays and Their Characterisation Techniques. *Def. Sci. J.* **2009**, *59* (6), 580–589. <https://doi.org/10.14429/dsj.59.1562>.
- (43) Sahoo, S.; Gaur, A. P. S.; Ahmadi, M.; Guinel, M. J. F.; Katiyar, R. S. Temperature-Dependent Raman Studies and Thermal Conductivity of Few-Layer MoS₂. *J. Phys. Chem. C* **2013**, *117* (17), 9042–9047. <https://doi.org/10.1021/jp402509w>.
- (44) Gu, X.; Li, B.; Yang, R. Layer Thickness-Dependent Phonon Properties and Thermal Conductivity of MoS₂. *J. Appl. Phys.* **2016**, *119* (8). <https://doi.org/10.1063/1.4942827>.
- (45) Bolduc, M.; Terroux, M.; Tremblay, B.; Marchese, L.; Savard, E.; Doucet, M.; Oulachgar, H.; Alain, C.; Jerominek, H.; Bergeron, A. Noise-Equivalent Power Characterization of an Uncooled Microbolometer-Based THz Imaging Camera; Anwar, M., Dhar, N. K., Crowe, T. W., Eds.; International Society for Optics and Photonics, 2011; Vol. 8023, p 80230C. <https://doi.org/10.1117/12.883507>.
- (46) Mather, J. C. Bolometer Noise: Nonequilibrium Theory. *Appl. Opt.* **1982**, *21* (6), 1125. <https://doi.org/10.1364/AO.21.001125>.

Supporting Information

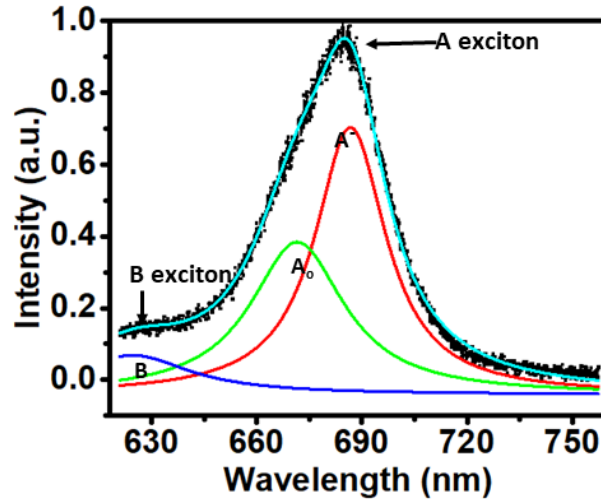


Figure S1. Photoluminescence (PL) spectra of MoS₂

The multilayer MoS₂ flake shows a very strong Photoluminescence (PL) peak centred around 689 nm with the asymmetric distribution (**Figure S1**). The Lorentzian peak fitting indicates the presence of the three distinct peaks at wavelengths 622.2 nm, 671.8 nm and 686.5 nm. The first two peaks are due to the existence of neutral excitons *B* and *A*₀ respectively, near the *K* point of the Brillouin zone boundary^{1,2}. These two excitons are expected to exist due to spin-orbit band splitting in the valence band and the interlayer coupling³. The third Lorentzian peak, observed at 686.5 nm, is associated with the trions (charged excitons), which is a three-particle system comprising of an exciton with an electron (or a hole), known as the negative (or positive) trion [4]. In PL spectra, negative trions (*T*) recombination is dominant which indicates the intrinsic n-type behaviour of MoS₂⁴.

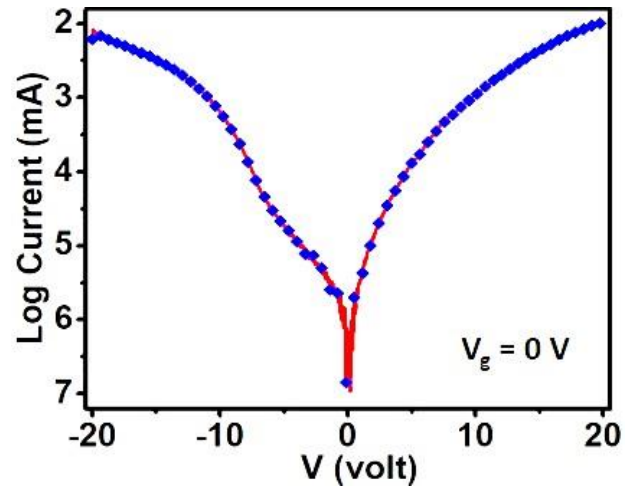


Figure S2. I-V characteristic of MoS₂ device in dark indicating the ohmic behaviour of the contact between flake and gold electrodes.

To investigate the nature of contact formed between the suspended flake and the electrodes, the output characteristics is plotted in semi-log scale for zero gate voltage, shown in **Figure S2**. The output current is almost identical and symmetric for both the forward and reverse bias, which indicate a good ohmic contact at the MoS₂-Au junction.

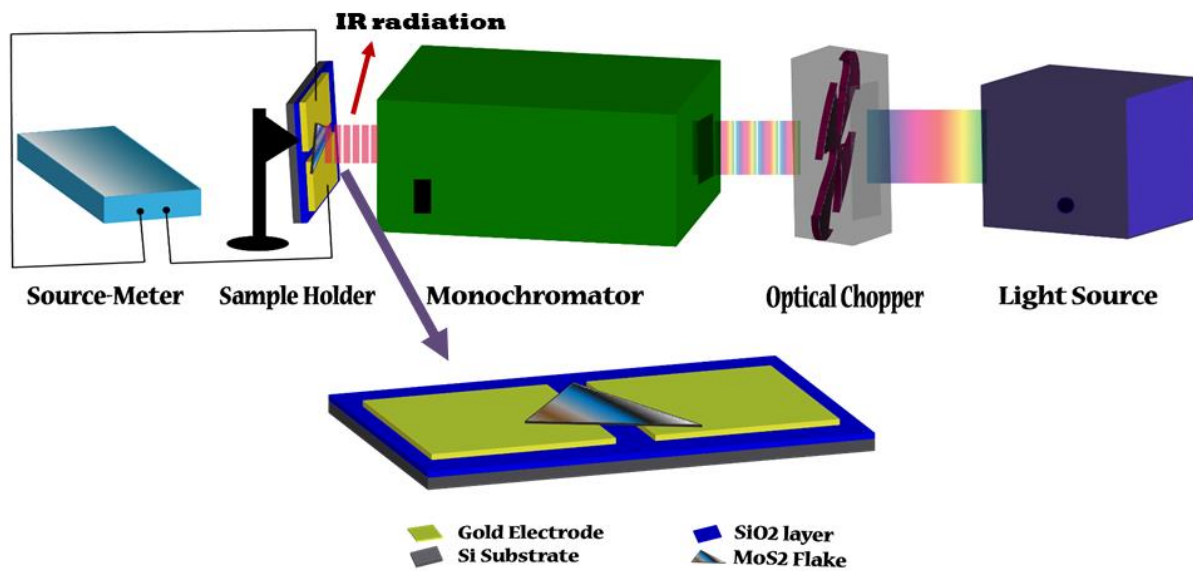


Figure S3. Schematic diagram for MoS₂ device and measurement set-up.

Figure S3 shows a schematic representation of the MoS₂ device and experimental set-up to examine the photo response of the device. A white-light beam from the light source is entered into the monochromator via passing through the optical chopper, which chopped the light at the desired frequency. A 900 nm IR wavelength is selected from the monochromator, incident on the MoS₂ flake and then corresponding I-V is measured by the source-meter connected to the sample by through the gold electrodes. Here the monochromator is kept 10 cm away from the device in ambient conditions and the incident radiation power at the device position is measured by a Si based power meter.

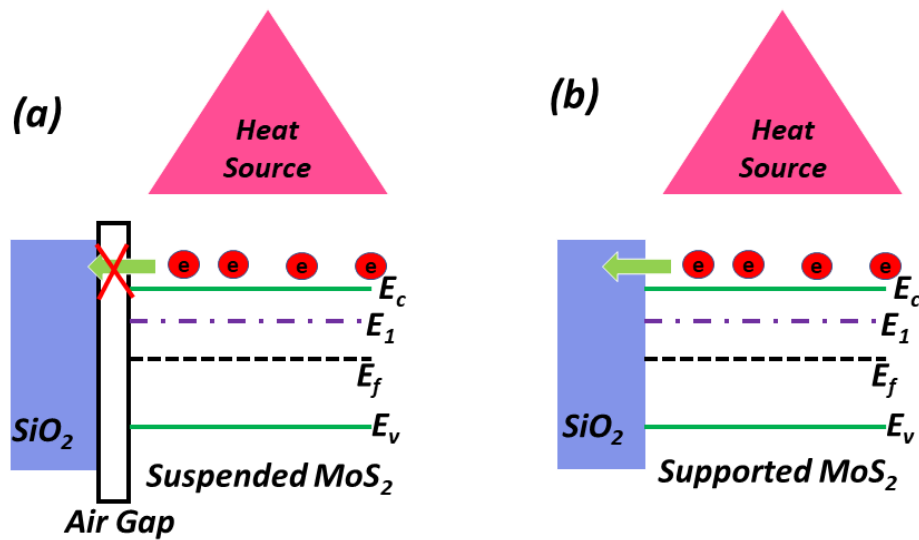


Figure S4. Band alignment of both suspended (a) and supported (b) MoS₂ device under IR illumination

To understand the mechanism behind the rise in the current upon NIR irradiation / heating, the band alignment of the device is sketched in **Figure S4**. Our experimental set up uniformly illuminates/warms-up the device so that there is no temperature gradient across the suspended MoS₂ flake and therefore, the possibility of thermoelectric effect can be ignored.

The charge carriers (electrons in the present case) gain some thermal energy from this heating process, which would equally be distributed among them. Such even rise in the temperature of the electrons lead to the reduction in the mean free path, and hence results in a significant drop in the material resistivity. We attribute this profound change in the resistivity with the suspended

geometry of our device as electrons cannot dissipate their heat energy towards the substrate, and so are giving rise the resistance variation with change in the temperature of the MoS₂ flake.

References

- (1) Coehoorn, R.; Haas, C.; Dijkstra, J.; Flipse, C. J. F.; de Groot, R. A.; Wold, A. Electronic Structure of MoSe₂, MoS₂, and WSe₂. I. Band-Structure Calculations and Photoelectron Spectroscopy. *Phys. Rev. B* **1987**, *35* (12), 6195–6202. <https://doi.org/10.1103/PhysRevB.35.6195>.
- (2) Coehoorn, R.; Haas, C.; de Groot, R. A. Electronic Structure of MoSe₂, MoS₂, and WSe₂. II. The Nature of the Optical Band Gaps. *Phys. Rev. B* **1987**, *35* (12), 6203–6206. <https://doi.org/10.1103/PhysRevB.35.6203>.
- (3) Splendiani, A.; Sun, L.; Zhang, Y.; Li, T.; Kim, J.; Chim, C. Y.; Galli, G.; Wang, F. Emerging Photoluminescence in Monolayer MoS₂. *Nano Lett.* **2010**, *10* (4), 1271–1275. <https://doi.org/10.1021/nl903868w>.
- (4) Mak, K. F.; He, K.; Lee, C.; Lee, G. H.; Hone, J.; Heinz, T. F.; Shan, J. Tightly Bound Trions in Monolayer MoS₂. *Nat. Mater.* **2013**, *12* (3), 207–211. <https://doi.org/10.1038/nmat3505>.